Development of Polarized High-Energy Photon Beams using Coherent Bremsstrahlung

William Livesay, Richard Jones, James McIntyre
Honors Advisor & Thesis Supervisor: Richard Jones

1 Abstract

The GlueX experiment at Jefferson Laboratory investigates exotic mesons produced through the interaction of high-energy gamma rays with protons in a liquid hydrogen target. These gamma rays are generated via bremsstrahlung, which also produces unwanted low-energy X-rays that contribute to background noise and signal pileup, limiting beam intensity and data quality. To address this, we designed a grazing-incidence mirror capable of reflecting X-rays while remaining transparent to the higher-energy gamma rays essential to the experiment. Minimizing both the thickness and surface roughness of the mirror is critical to achieving this energy selectivity. Preliminary testing suggests that thin films behave similarly to their thicker counterparts, with only small variations observed. However, additional trials and improved experimental methods are required to assess the presence of any non-ideal effects with any confidence.

Contents

2 Introduction

The GlueX experiment is located at Jefferson Laboratory and has four unique halls. One major experiment in Hall D is to use photoproduction from a collision between gamma rays and protons in a liquid hydrogen target to create exotic mesons. In order to make a reaction capable of producing these exotic mesons, gamma rays are essential.

The method of creating gamma rays is bremsstrahlung, where electrons emit photons of various energies while slowing in a medium. The GlueX experiment uses gamma rays primarily in the range of 8.4-9 GeV for photoproduction of various hadronic particles. Although the primary energies used lie in this range, gamma rays of 6.3-8 GeV are used as well. Therefore, photons of 6 GeV and below only contribute as background. Unfortunately, to produce gamma rays of the desired energy through bremsstrahlung, lower energy photons known as X-rays are also created, limiting how intense the photon beam can be without overwhelming the capabilities of the electronics to handle the signal rates. The resulting pileup effect of multiple photons that cannot be distinguished separately complicates the data analysis.

The goal of this work is to create a small, lightweight grazing incidence mirror that can reflect lower-energy X-rays and remove them from the photon beam while remaining transparent to the higher-energy gamma rays. This mirror should be sufficiently thin to avoid absorbing useful gamma rays as described in Section 3.1. The angle of incidence will be a grazing angle because a decrease in angle increases the reflectivity for photons of all energies. Careful choice of this angle is essential to reflect undesired photons and transmit desired ones, discussed in Section 5.4.

The overall objective is to create a sufficiently planar and smooth surface that is capable of filtering enough of the X-rays while at the same time keeping its material thickness to a minimum, on the order of one micron. The mirror will be held at grazing incidence to raise the 'cutoff' photon energy to the few hundred keV range. The physical space available in the GlueX detector beamline is limited, so a mirror with minimal size is ideal. The principal challenge lies in reducing the roughness of the mirror, as roughness decreases the reflectivity of photons, making the mirror less effective in filtering out X-rays as described later by Section 5.2 and Figure 13 [6].

3 Theoretical Framework

3.1 Absorption in Media

The Beer-Lambert law describes the attenuation of light as it passes through an absorbing medium. It is given by:

$$\frac{I}{I_0} = e^{-\mu x} \tag{1}$$

where I/I_0 is the ratio of the transmitted intensity to the initial intensity of light (unitless), μ is the linear attenuation coefficient (m^{-1}) of the material, and x is the path length of the photon in the material (m).

3.2 Complex X-ray Refractive Indices

The refractive index n_r for X-rays in a material is a complex value:

$$n_r = 1 - \delta + i\beta \tag{2}$$

where: n_r is the complex refractive index of the material, δ is the dispersion coefficient, and β is the the attenuation coefficient.

The refractive index is a measure of how much the X-ray beam is bent as it travels through a medium, with δ affecting the phase velocity of the X-rays, and β accounting for the loss of intensity due to scattering and absorption.

For X-rays in matter, the refractive index can be approximated as:

$$n_r = 1 - \frac{r_\mathbf{c}}{2\pi}\lambda^2 \sum_j n_{atom,j} f_j \tag{3}$$

where: $r_\mathbf{c}$ is the classical electron radius, approximately 2.8179×10^{-15} m, λ is the wavelength of the X-ray (m), $n_{atom,j}$ is the number density of atoms of type j (atoms/m^3), f_j is the atomic form factor for element j. The summation $\sum_j$ accounts for contributions from different atomic species in the material. For a material that consists of only one homogeneous type of atom, the equation for n_r simplifies significantly:

$$n_r = 1 - \frac{r_c}{2\pi}\lambda^2 n_{\text{atom}} f_{tot} \tag{4}$$

For a single element or homogeneous material, the atomic form factor f can be divided into two components:

$$f_{\text{tot}} = f_1 + i f_2 \tag{5}$$

where f_1 is the real part of the atomic scattering factor, representing the dispersion, and f_2 is the imaginary part related to absorption.

Now, let us define n_{atom} in terms of the material density ρ (kg/m^3), Avogadro's number N_A, and the atomic mass A (kg/mol). The number density is given by:

$$n_{\text{atom}} = \frac{\rho N_A}{A}, \tag{6}$$

where $N_A = 6.02214076 \times 10^{23}$ atoms/mol. Substituting this expression for n_{atom} into the refractive index equation gives the following:

$$n_r = 1 - \frac{r_\mathbf{c}}{2\pi}\lambda^2 \frac{\rho N_A}{A}(f_1 + i f_2). \tag{7}$$

Thus, for a homogeneous material, the refractive index n_r depends on the wavelength of the X-rays and the density, atomic mass, and atomic form factors of the material.

Separating this back into the original form of Equation 2, we determine the values of δ and β to be:

$$\delta = \frac{r_\mathbf{c}}{2\pi}\lambda^2 \frac{\rho N_A}{A} f_1 \tag{8}$$

$$\beta = \frac{r_\mathbf{c}}{2\pi}\lambda^2 \frac{\rho N_A}{A} f_2 \tag{9}$$

This model is valid primarily for X-ray energies (typically below $\sim$1 MeV) as at higher energies nuclear physics effects dominate and atomic form factors are no longer applicable.

3.3 Reflectivity and Roughness

The reflectivity of a surface is defined as the ratio of reflected photons to the total number of incident photons. This quantity depends on the photon energy, the angle of incidence, and the refractive index of the material. For a smooth interface between two media, the reflectivity R is described by the Fresnel equations, which govern the reflection and refraction of electromagnetic waves at the boundary. These equations treat the electric field components separately for polarization perpendicular (s-polarization) and parallel (p-polarization) to the plane of incidence.

X-ray Reflectivity

For an incident wave with angle θ_i (measured from the surface normal), the amplitude reflection coefficients are:

$$r_s = \frac{n_1 \cos\theta_i - n_2 \cos\theta_t}{n_1 \cos\theta_i + n_2 \cos\theta_t} \qquad \text{(s-polarization)}, \tag{10}$$

$$r_p = \frac{n_2 \cos\theta_i - n_1 \cos\theta_t}{n_2 \cos\theta_i + n_1 \cos\theta_t} \qquad \text{(p-polarization)}, \tag{11}$$

where: n_1, n_2 are the complex refractive indices of the two media and θ_t is the angle of refraction, given by Snell's law: $n_1 \sin\theta_i = n_2 \sin\theta_t$.

The reflectivity for each polarization is:

$$R_s = |r_s|^2, \tag{12}$$

$$R_p = |r_p|^2. \tag{13}$$

Finally, for unpolarized light, the average reflectivity is:

$$R = \frac{R_s + R_p}{2}. \tag{14}$$

The following equation describes the critical angle, the angle for which any smaller angle causes the given photons to exhibit total internal reflection on a perfectly smooth surface:

$$\theta_c \approx \sqrt{2\delta}. \tag{15}$$

The critical angle is a function of the dispersion coefficient, which depends on the energy of photon being reflected.

Roughness Component

Roughness supplies a Gaussian probability distribution for the angle of incidence that reduces the average reflectivity at all angles, including those below the critical angle.

Specifically, surface roughness σ, Root Mean Squared (RMS) height, reduces reflectivity via the Névot-Croce factor [7]:

$$R_{\text{rough}} = R_{\text{ideal}} \cdot e^{-(4\pi\sigma \sin\theta_i/\lambda)^2}, \tag{16}$$

3.4 Differential Thermal Expansion

The expansion or contraction of a material is given by:

$$\frac{\Delta L}{L_0} = (T_2 - T_1) \cdot \alpha_i \tag{17}$$

where α_i is the Coefficient of Thermal Expansion (CTE) of material i, $\Delta L/L_0$ is the ratio of the change in length to the initial length (unitless), and T_j is the temperature at time j (°C). When two materials are fixed together in a certain way, their relative expansions or contractions may interfere with each other. In the case where $\alpha_1 > \alpha_2$ and $T_1 > T_2$, the contraction of material 2 limits the overall contraction. Therefore, for a system with material 2 surrounding material 1 in all directions at the boundary, we have:

$$\frac{\Delta L_{diff}}{L_0} = (T_2 - T_1) \cdot (\alpha_1 - \alpha_2) = \epsilon \tag{18}$$

where ϵ is the thermal strain due to a CTE mismatch. The resulting tension T in the membrane is related to the strain by Hooke's law:

$$\sigma = E \cdot \epsilon = \frac{T}{h} \tag{19}$$

where E is Young's modulus of the membrane and h is the thickness of the membrane. Young's modulus for a material is only valid for the linear regime, well below the yield and ultimate limits. Substituting Equation 17 into the expression for tension:

$$T = h\,E \cdot (T_2 - T_1)(\alpha_1 - \alpha_2) \tag{20}$$

3.5 Tension–Mass Relationship in Circular Membranes

Consider a flat circular membrane of radius R that is fixed at its edge and deformed by placing a mass m on it as shown in Figure 1. The load is evenly distributed along a circle smaller than the membrane, with no contact at the membrane's center. The weight of the mass causes the membrane to sag, forming a flat central region beneath the mass and an angled transition region that extends to the boundary. At the edge of the flat region (radius r), the membrane forms an angle θ with the horizontal.

We seek to determine the tension T (in N/m) required in the membrane to support the mass in static equilibrium.

Calculating Membrane Tension

Under load, the membrane responds with an upward force from the vertical components of the tension at the circular boundary between the flat and angled regions. Each infinitesimal element of the boundary contributes a vertical force:

$$dF_{\mathrm{y}} = dF_A \sin\theta = T\,ds \sin\theta$$

where, as shown in Figure 1, θ is the angle between the horizontal angled portion of the membrane, dF_y is the vertical component of the angled force dF_A, $ds = R\,d\phi$ is the arc length of the infinitesimal segment at radius R, and ϕ is the azimuthal angle around the circle.

Integrating over the full circle gives the total vertical restoring force:

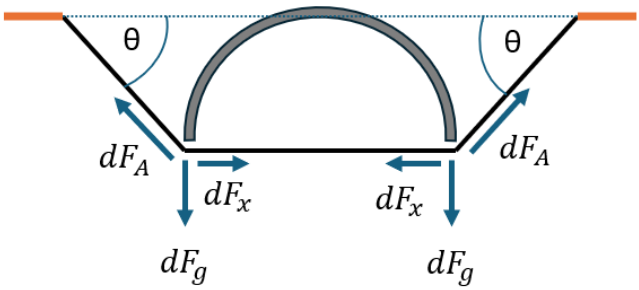

Figure 1: Side view diagram of membrane force vectors at the contact point with the load.

$$F_y = \int_0^{2\pi} T \sin\theta R \, d\phi = 2\pi RT \sin\theta$$

At equilibrium, the vertical component of the tension must balance the gravitational force.

$$2\pi RT \sin(\theta) = mg$$

Solving for the tension:

$$T = \frac{mg}{2\pi R \sin(\theta)}$$

This relation shows that the required membrane tension increases with mass m and decreases with both the radius R and the angle θ between the membrane and the horizontal at the transition boundary. The tension becomes large as $\theta \to 0$, where the vertical component of the membrane force vanishes.

3.6 Vibration of a Circular Membrane

We begin with the expression for the force along a small element of the membrane. The differential force dF is related to the tension T and the differential length dl of the membrane element:

$$dF = T \, dl \tag{21}$$

For a flat circular membrane, the tension varies with both the radial and angular directions. We consider a trapezoid height dr and thickness $d\theta$ with its small base closest to the origin. We first consider the radial component of the force where the differential length dl is the length of the upper and lower sides of a trapezoid as shown in Figure 2.

$$dl = r \, d\theta \tag{22}$$

Thus, the radial force differential becomes the following:

$$dF = T \, r \, d\theta \tag{23}$$

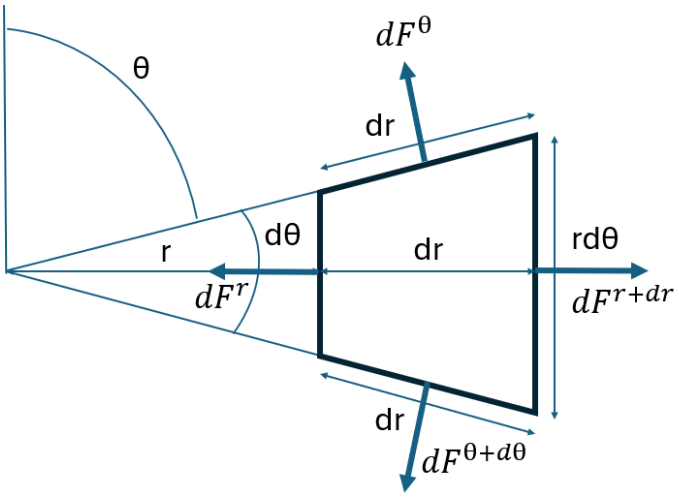

Figure 2: Diagram of small piece of circular membrane and its opposing force vectors.

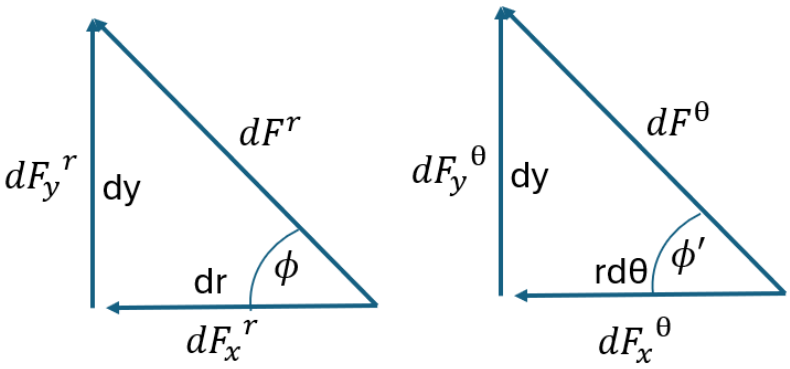

Figure 3: Diagrams of vertical and horizontal components of the force vectors in terms of angles ϕ and ϕ'.

where θ is the azimuthal angle. The horizontal components of the radial and azimuthal forces cancel, so we focus on the vertical component.

$$dF_y^{(r)} = T \sin\phi \, r \, d\theta \approx T \left(\frac{dy}{dr}\right) r \, d\theta \tag{24}$$

where ϕ is the angle above the membrane with respect to the horizontal as shown in Figure 3. Since for small angles: $\sin\phi \approx \tan\phi$, we have $\sin\phi \approx \frac{dy}{dr}$.

This expression gives the vertical force from one radial side of a differential element at a fixed angle θ. To find the net vertical force, we consider two opposing radial edges: one at r and the other at $r + dr$. The vertical force on the side at r is:

$$dF_y^{(r)} = T \left(\frac{\partial y}{\partial r}\bigg|_r\right) r \, d\theta \tag{25}$$

The vertical force on the side at $r + dr$ is:

$$dF_y^{(r+dr)} = T\left(\left.\frac{\partial y}{\partial r}\right|_{r+dr}\right)(r+dr)\,d\theta \tag{26}$$

The net vertical force in the radial direction is the difference:

$$dF_y^{(r,\text{net})} = T\left[\left(\left.\frac{\partial y}{\partial r}\right|_{r+dr}\right)(r+dr) - \left(\left.\frac{\partial y}{\partial r}\right|_{r}\right)r\right]d\theta \tag{27}$$

Multiplying out the terms:

$$= T\left[r\left(\left.\frac{\partial y}{\partial r}\right|_{r+dr} - \left.\frac{\partial y}{\partial r}\right|_{r}\right) + dr\left(\left.\frac{\partial y}{\partial r}\right|_{r+dr}\right)\right]d\theta \tag{28}$$

Now, using the definition of a derivative:

$$\frac{\partial}{\partial r}\left(\frac{\partial y}{\partial r}\right) = \lim_{dr\to 0}\frac{\left(\left.\frac{\partial y}{\partial r}\right|_{r+dr} - \left.\frac{\partial y}{\partial r}\right|_{r}\right)}{dr} \tag{29}$$

So substituting this equation in for the first two terms, we get:

$$dF_y^{(r,\text{net})} = T\left(r\frac{\partial^2 y}{\partial r^2} + \frac{\partial y}{\partial r}\right)dr\,d\theta \tag{30}$$

This is the net vertical force contribution from the radial direction. Now, we consider the angular components:

$$dF^{\theta} = Tdl \tag{31}$$

The angular components consider the two sides of the trapezoid both of length dr as shown in Figure 2.

$$dl = dr \tag{32}$$

$$dF^{\theta} = Tdr \tag{33}$$

$$dF_y^{(\theta)} = T\,\sin\phi\,dr \tag{34}$$

We can use the triangle on the right of Figure 3 going out of the page of Figure 2 with small angle ϕ', height dy, and base $r\,d\theta$ as we travel along the thickness of the trapezoid. So,

$$\sin\phi' \approx \tan\phi' = \frac{1}{r}\frac{\partial y}{\partial\theta} \tag{35}$$

and as before, we calculate the vertical component of this force:

$$dF_y^{(\theta)} = T\,\sin\phi'\,dr \approx T\,dr\cdot\left(\frac{1}{r}\frac{\partial y}{\partial\theta}\right) \tag{36}$$

Using this result for one side of the piece of membrane of thickness $rd\theta$, we find the net vertical force from the azimuthal direction in a similar way to the radial one:

Next, we subtract the values at θ and $\theta + d\theta$:

$$dF_y^{(\theta,\text{net})} = T\,\frac{1}{r}\,dr\,\left[\left(\left.\frac{\partial y}{\partial\theta}\right|_{\theta+d\theta}\right) - \left(\left.\frac{\partial y}{\partial\theta}\right|_{\theta}\right)\right] \tag{37}$$

Simplify the expression using the same definition of the derivative as before:

$$dF_y^{(\theta,\text{net})} = T\,\frac{1}{r}\,dr\,d\theta\left(\frac{\partial^2 y}{\partial\theta^2}\right) \tag{38}$$

Adding both contributions gives the total vertical force on the differential area element dA:

$$dF_y = T\left(r\frac{\partial^2 y}{\partial r^2} + \frac{\partial y}{\partial r} + \frac{1}{r}\frac{\partial^2 y}{\partial\theta^2}\right)dr\,d\theta \tag{39}$$

The area of the membrane piece can be found by:

$$dA = r\,dr\,d\theta \tag{40}$$

Factoring out dA, we get the following:

$$dF_y = T\,dA\left(\frac{\partial^2 y}{\partial r^2} + \frac{1}{r}\frac{\partial y}{\partial r} + \frac{1}{r^2}\frac{\partial^2 y}{\partial\theta^2}\right) \tag{41}$$

This is the expression for the net vertical force acting on a small patch of the circular membrane due to tension in both the radial and angular directions. The expression in parentheses is the Laplacian in polar coordinates acting on y, denoted $\nabla^2 y$:

$$\nabla^2 y = \frac{\partial^2 y}{\partial r^2} + \frac{1}{r}\frac{\partial y}{\partial r} + \frac{1}{r^2}\frac{\partial^2 y}{\partial\theta^2} \tag{42}$$

So, the vertical force becomes:

$$dF_y = T\,dA\,\nabla^2 y \tag{43}$$

From Newton's second law, we have the following:

$$dF_y = \ddot{y}\cdot dm \tag{44}$$

The mass of the element is equal to $\sigma\,dA$, where σ is the mass per unit area. Therefore,

$$\ddot{y}\,\sigma\,dA = T\,dA\,\nabla^2 y \tag{45}$$

$$\sigma\,\ddot{y} = T\,\nabla^2 y \tag{46}$$

Finally, we write the wave equation for a circular membrane:

$$\ddot{y} = \frac{T}{\sigma}\,\nabla^2 y \tag{47}$$

Letting $v^2 = \frac{T}{\sigma}$, we get the standard form:

$$\ddot{y} = v^2\nabla^2 y \tag{48}$$

This is the general form of the wave equation for the circular vibrating membrane. We now assume a solution of the following form:

$$y(r,\theta,t) = R(r)\Phi(\theta)T(t) \tag{49}$$

where $R(r)$ is the radial component of displacement, $\Phi(\theta)$ is the angular component, and T(t) is the time component. Substituting this assumed solution into the wave equation and separating the variables gives the following equation:

$$\frac{1}{v^2T}\frac{d^2T}{dt^2} = \frac{1}{R}\frac{d^2R}{dr^2} + \frac{1}{rR}\frac{dR}{dr} + \frac{1}{r^2\Theta}\frac{d^2\Theta}{d\theta^2} = K \tag{50}$$

Both sides of this equation must be equal to a constant K, as they depend on different variables. First, we solve the time component:

$$\frac{d^2T}{dt^2} = Kv^2T \tag{51}$$

We know the wave speed $v \geq 0$, but the time component must oscillate and not diverge or converge to 0 as damping effects are not considered here. Therefore, we can assume that K is negative: $K = -k^2$ for positive spatial frequency k. We arrive at the following solution for the time component:

$$T(t) = A\sin vkt + B\cos vkt \tag{52}$$

Using the initial condition of an initial height of 0 across the membrane, we get:

$$T(t) = \sin vkt \tag{53}$$

where the constant A will get absorbed by others in the final solution. Next, we look at the remaining components:

$$\frac{1}{R}\frac{d^2R}{dr^2} + \frac{1}{rR}\frac{dR}{dr} + \frac{1}{r^2\Theta}\frac{d^2\Theta}{d\theta^2} = -k^2 \tag{54}$$

Rearranging,

$$\frac{r^2}{R}\frac{d^2R}{dr^2} + \frac{r}{R}\frac{dR}{dr} + k^2r^2 = -\frac{1}{\Theta}\frac{d^2\Theta}{d\theta^2} = L \tag{55}$$

We now have a similar situation where two components are separated within the equation and must be constant. We can now solve for the azimuthal dependence using the same method as we did for time. We arrive at the following.

$$\Theta(\theta) = C\cos m\theta + D\sin m\theta \tag{56}$$

with $L = m^2$. m is a positive integer that represents the mode of oscillation.

Next, for the radial part, we obtain the following ordinary differential equation:

$$\frac{r^2}{R}\frac{d^2R}{dr^2} + \frac{r}{R}\frac{dR}{dr} + k^2r^2 = m^2 \tag{57}$$

$$r^2\frac{d^2R}{dr^2} + r\frac{dR}{dr} + (k^2r^2 - m^2)R = 0 \tag{58}$$

This is a form of the Bessel equation, and the solution to this equation is given by the Bessel function of the first kind $J_m(r)$. Thus, the radial solution is as follows:

$$R(r) = A_1J_m(kr) + A_2Y_m(kr) \tag{59}$$

We can assume that the coefficient Y_m is zero because it diverges for $r = 0$, which cannot be true at the center of our membrane. Therefore, we have the following:

$$R(r) = J_m(kr) \tag{60}$$

where the will again be absorbed later on. Now, using the boundary condition of:

$$y(a, \theta, t) = 0 \tag{61}$$

where a is the outer radius, we have

$$R(a) = J_m(ka) = 0 \tag{62}$$

$$k_{mn} = \frac{\alpha_{mn}}{a} \tag{63}$$

where α_{mn} is the nth root of J_m or the spatial mode number for a discrete radial mode number n and the azimuthal mode number m. Finally, the solution for the membrane displacement is

$$y_{mn}(r, \theta, t) = J_m\left(\frac{\alpha_{mn}}{a} r\right) \sin(\frac{\alpha_{mn}}{a} vt) \left[C_1 \sin(m\theta) + C_2 \cos(m\theta)\right] \tag{64}$$

where the solution assumes that the membrane is undergoing exactly one mode corresponding to integers n and m at different frequencies:

$$\omega_{mn} = v\frac{\alpha_{mn}}{a} \tag{65}$$

where ω_{mn} is the frequency of resonant mode (n, m) in rad/s. Substituting ν back in we get the following relation between frequency of oscillation and tension of a vibrating circular membrane bound at its edge initially at rest on the horizontal for distinct resonant modes:

$$\omega_{mn} = \frac{\alpha_{mn}}{a}\sqrt{\frac{T}{\sigma}} \tag{66}$$

3.7 Variable Capacitor Current

Consider a parallel-plate capacitor with a time-dependent plate separation $d(t)$, given by:

$$d(t) = d_0 + h\sin(\omega t), \tag{67}$$

where d_0 is the equilibrium separation, h is the oscillation amplitude ($h \ll d_0$), and ω is the angular frequency of oscillation. The capacitance $C(t)$ is:

$$C(t) = \frac{\epsilon A}{d(t)} = \frac{\epsilon A}{d_0 + h\sin(\omega t)}, \tag{68}$$

where ϵ is the permittivity of the dielectric and A is the plate overlap area.

When the capacitor is connected to a constant DC voltage source V, the charge $Q(t)$ on the plates varies with time:

$$Q(t) = C(t)V = V\frac{\epsilon A}{d_0 + h\sin(\omega t)}. \tag{69}$$

The current $I(t)$ is the time derivative of the charge:

$$I(t) = \frac{dQ(t)}{dt} = V\epsilon A \frac{d}{dt}\left(\frac{1}{d_0 + h\sin(\omega t)}\right). \tag{70}$$

Evaluating the derivative yields:

$$\frac{d}{dt}\left(\frac{1}{d_0 + h\sin(\omega t)}\right) = -\frac{h\omega\cos(\omega t)}{[d_0 + h\sin(\omega t)]^2}. \tag{71}$$

Thus, the current is:

$$I(t) = -V\epsilon A \frac{h\omega\cos(\omega t)}{[d_0 + h\sin(\omega t)]^2}. \tag{72}$$

For small oscillations ($h \ll d_0$), the denominator can be approximated as d_0^2, simplifying the expression to:

$$I(t) \approx -VC_0 \frac{h\omega}{d_0}\cos(\omega t), \tag{73}$$

where $C_0 = \epsilon A/d_0$ is the equilibrium capacitance.

3.8 Amplifier Electronics

The electronic amplifier increases the output signal by different orders of magnitude, depending on the selected gain level. The gain is controlled using Transistor-Transistor Logic (TTL) signals. Three TTL input wires each accept voltage levels of 0–0.8 V to represent logic 0 and 2–5 V to represent logic 1. Together, these three inputs form a 3-bit binary word, allowing control of gain levels from 0 to 7. The range selection consists of 10^{-6} through 10^{-12} A/V.

4 Methodology

4.1 Method of Decreasing Roughness

Sections 3.1 and 5.4 describe the need for a minimal thickness and roughness of the membrane. With this goal in mind, these limitations go hand in hand to form a difficult problem. Mechanical methods of stretching any material would immediately tear the thin membrane. Therefore, differential thermal expansion is the preferred method for reducing roughness. Using differences in the CTE in materials, tension can be applied through a change of temperature to stretch and smooth the membrane. The desired system consists of a high-CTE material that makes up the membrane and a low-CTE material that serves as a boundary for this membrane. After the materials are fixed together, any decrease in temperature will induce tension from the membrane's compression being greater than the boundary's.

With this in mind, aluminum has a CTE of $(23.5 \pm 0.3) \times 10^{-6}\,^{\circ}\mathrm{C}^{-1}$ for certain changes in temperature (from 20°C to 100°C) [9]. This relatively high value contrasts with cast iron's: $(10.7 \pm 0.3) \times 10^{-6}\,^{\circ}\mathrm{C}^{-1}$ [3]. The discrepancy in the CTE values, availability, and cost of these materials makes them the primary choices for the membrane and boundary for this work.

4.2 Differential Thermal Expansion

Equation 20 describes the tension created by differential thermal expansion. The expression shows that the tension is directly proportional to both the temperature change and the difference in the CTE values between the membrane and the boundary. From this relationship, in order to achieve maximum tension for a minimum temperature change, the maximum difference in CTE is essential.

It is important to note that some assumptions were made in the analysis of this relationship. In order to use Young's modulus, the strain must be in the linear regime (far from the yield limit), and the deformation must be uniaxial. In the case of a circular membrane, the deformation is biaxial, so analysis using Poisson's ratio is needed. However, further calculation of the tension created by specific CTE and temperature changes is rigorous and potentially fruitless as there are likely many unaccounted for factors with unknown contributions, especially for thin membranes. Therefore, this analysis is paused here and pivoted to experimental methods.

4.3 Initial Experimental Design

Since there are limitations to the precision of theoretical calculations of the tension that a membrane undergoes experimentally, learning about how thin membranes act under high amounts of tension compared to theory is crucial. From this point of view, applying tension mechanically to a slightly thicker aluminum membrane can provide information about the thinner membrane while being more practical and efficient.

Figure 4: Top and side views of the original rung used to border the membrane.

The test material chosen is 16 micron thick standard kitchen aluminum foil for convenience and material continuity with the actual membrane. The first setup consists of a hollow metal hoop with a radius of 11.5 cm as shown in Figure 4. The original setup is shown in Figure 5. DP-420 epoxy was chosen to secure the membrane to the hoop due to its strength and heat resistance if heat is later used. Epoxy was applied by hand to the outer edge of the top of the hoop. The hoop was carefully flipped and placed on the

membrane, and it was left to cure. This process was later optimized for the symmetry and strength of the epoxy and membrane.

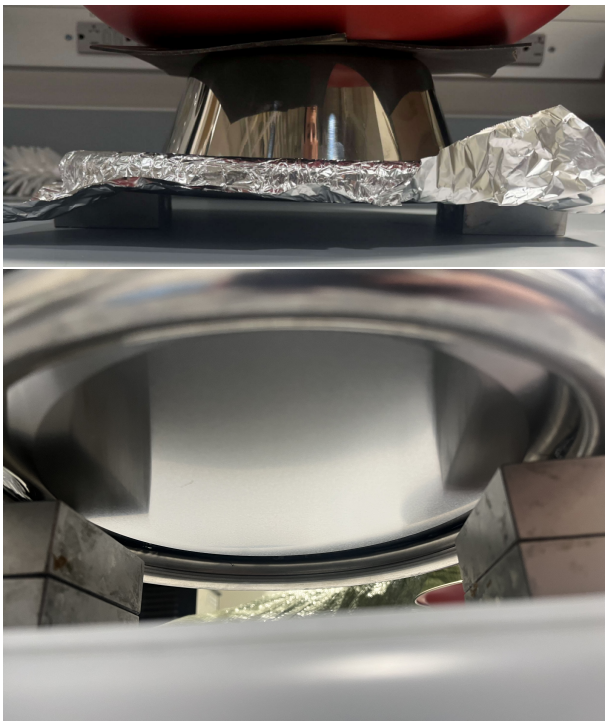

Figure 5: Side and bottom views of the original mechanical tension setup.

The system is laid on supports with the membrane still facing upwards. A bowl with a flat rim of radius 5.7 cm and a flat bottom (seen in the upper part of Figure 5) is placed upside down on the center of the circular membrane as the method of applying tension. Then, a much larger bowl is placed right-side up to provide a greater volume for adding more weight. Steel ballast was chosen as the main weight supplier due to its density and small increments. The steel ballast was poured very slowly and carefully in the center of the larger bowl for approximately half an hour until the membrane ripped. This process was followed twice, but the amount of mass supported by the membrane was 25 kg and 14 kg, respectively, for the two trials. This drastic variation further suggests that there are unaccounted factors compounding to alter the strength of the membrane from trial to trial. Despite careful recreation, with the current setup sharp epoxy edges and asymmetry is inevitable.

4.4 Improved Experimental Design

To improve the reproducibility of the tests, more care was put into the components of the setup and the assembly process.

First, a dual-cartridge epoxy dispenser was used as a more consistent method to apply the epoxy. The application was more precise in location and quantity, which reduced epoxy overflow, uneven application, or sharp edges. These factors make aluminum less susceptible to unintentional damage and maintain the azimuthal symmetry of the system as much as possible.

Second, a thin, flat copper ring with slightly rounded edges was used in place of the metal hoop, which arrived slightly dented and misshapen. The copper, shown on the

upper left of Figure 6, appears perfectly flat to the eye, which helps with symmetry and epoxy application. Although it can maintain extreme tension in the horizontal direction, the main drawback of the copper ring is its limited capacity to support forces in the vertical direction.

The third major change helps solve this issue and stabilize the entire system. Rather than small, disconnected blocks supporting the system, a 1/2" thick wooden plank had a hole removed from the center to place the copper on and serve as a support and table for the experiment. This plank is depicted on the top right and bottom right of Figure 6. Flat legs were then securely screwed in to ensure that no tilting would occur, which could disrupt symmetry.

Figure 6: Photos of the copper hoop (top left), aluminum membrane (top right), bowl with steel ballast (bottom left), and antenna (bottom right).

4.5 Measurement of Membrane Tension

Despite improving the system to maximize the strength and symmetry of the membrane, the unknown factors associated with the strength of thin films under high tension remain. A method of measuring the membrane tension for a given load mass would be informative. The chosen non-contact method of measuring tension is acoustic excitation and capacitive sensing.

4.5.1 Acoustic Membrane Excitation

The relationship between tension and frequency of oscillation for various modes of a circular membrane described by Equation 66 is used to find tension. A large speaker pictured in Figure 7 is used to excite the membrane over a wide range of frequencies. Somewhere along the frequency sweep, the membrane will vibrate in a pattern with a unique symmetry depending on the vibration mode, as seen in Figure 8. The final step

is to be able to differentiate between these patterns despite the high frequency and low amplitude of motion, making visual determination unrealistic.

Figure 7: Image of large speaker used for excitation.

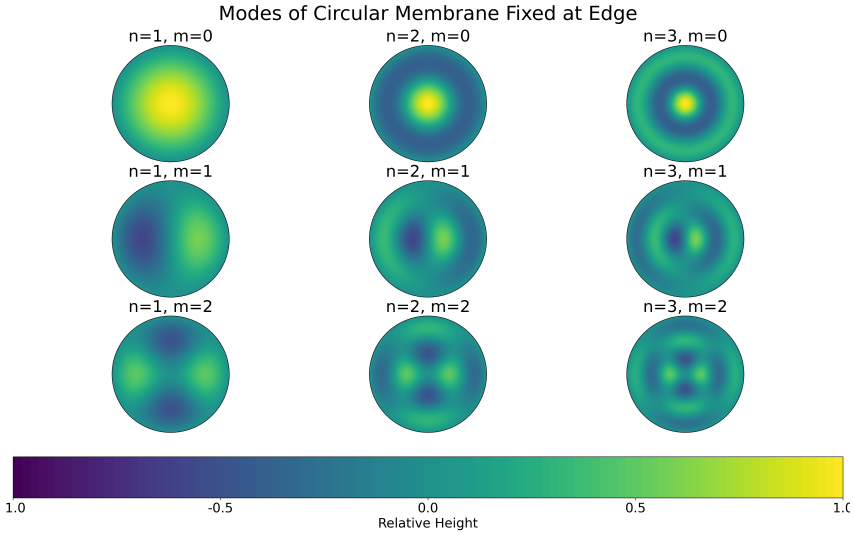

Figure 8: Height profiles of resonant modes (1,0) through (3,2) of a circular membrane with a fixed edge.

4.5.2 Circuit Design

To this end, a circuit was designed with the main function of measuring the frequency for which the membrane reaches its maximum amplitude at its center. This frequency is the (1,0) mode, also known as the fundamental frequency. As seen in Figure 8, the (1,0) mode has azimuthal symmetry and has the largest amplitude of any other mode for a constant volume level of excitation. Since frequencies between modes are combinations of these pure modes, the (1,0) mode must have the largest amplitude at the center. Therefore, locating the frequency for which the amplitude is at a maximum will find the fundamental frequency.

This is done by using the membrane as a plate of a mechanically modulated capacitor. The other plate of the capacitor is a stationary tin-coated steel sheet electrode charged with 15 V of DC voltage. The fixed plate is held a couple millimeters away from the membrane to detect its motion effectively. For a better view to confirm the distance between the antenna and the membrane, a small Raspberry Pi camera is hot-glued to the inner edge of the hole in the wooden plank. Both the antenna and camera are shown in Figure 9.

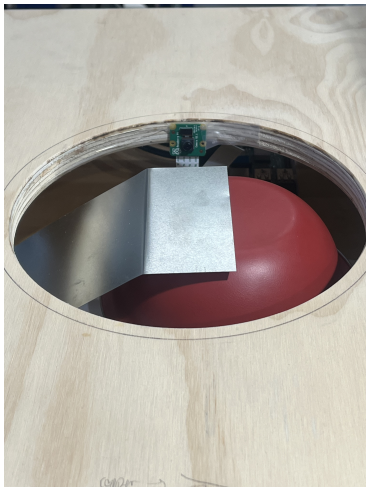

Figure 9: Image of Raspberry Pi camera viewing antenna position.

The oscillation of the membrane causes the capacitance to vary periodically. This time-varying capacitance creates a displacement current that effectively acts as an AC current generated across the capacitor terminals according to Equation 73 due to its approximate pure sinusoid nature. The varying capacitance forces the battery to supply or absorb charge to maintain a constant voltage.

As shown in Figure 10 (left), the current signal appears in a parallel RC circuit with a resistance of 1 MΩ and a capacitance of 1μF. This creates a time constant of $\tau = 1$ s. The RC circuit allows AC fluctuations to develop across the capacitor without significant attenuation. This filtering ensures that the slowly varying DC offset is decoupled from the high-frequency signal.

4.5.3 Amplifier Electronics

The electronic amplifier, described in Section 3.8, is added to the circuit to amplify the current being measured. The gain is adjusted using TTL levels, which are controlled using 3 2x2 headers to switch between logic 0 and logic 1 for each wire. 2 pins of each header are supplied with an ideal voltage of 5.07 V created by a voltage divider shown in Figure 10 (left), while the other 2 are grounded. The remaining function of the circuit is to properly power the electronic amplifier.

The electronic amplifier will amplify the signal and send it to the oscilloscope to be read and analyzed. The spikes in the resulting voltage graph indicate a greater change in capacitance, a greater membrane displacement at its center, and therefore a pure, likely $m = 0$, mode. The largest and first spike should correspond to the fundamental frequency when moving from low to high frequencies.

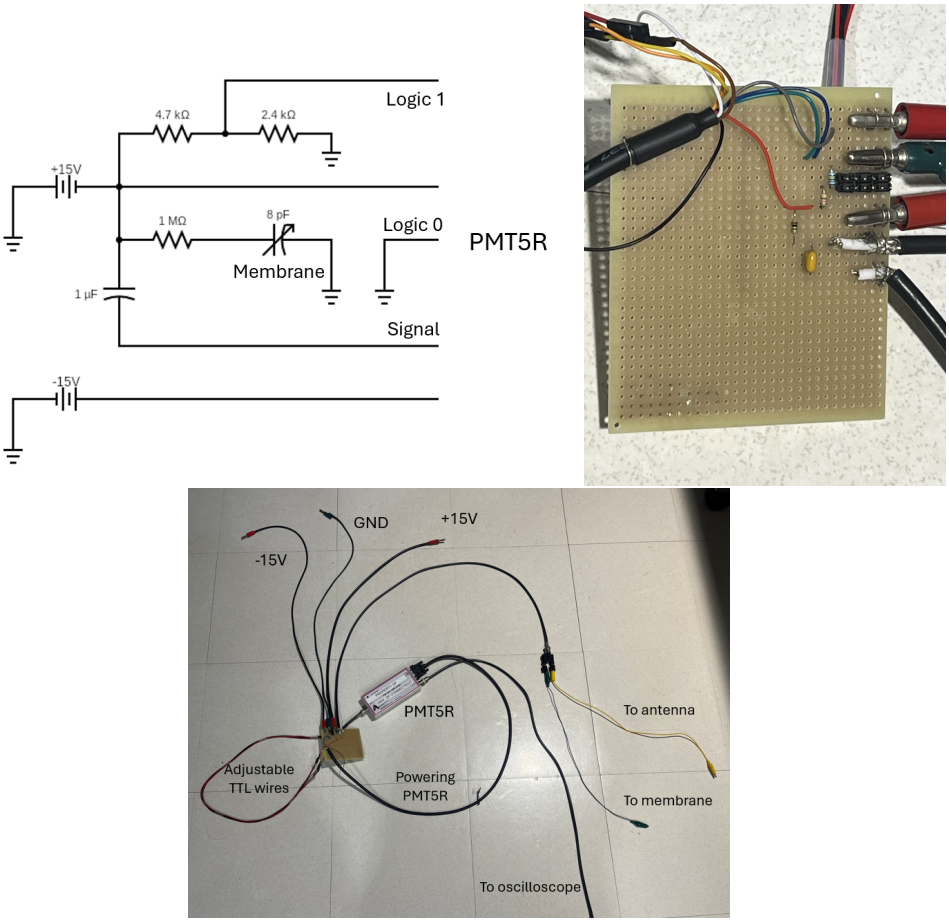

Figure 10: Circuit diagram (left), circuit image (right), and wire layout (bottom) with signal decoupling, PMT5R gain control, and PMT5R powering.

5 Computational Methods

5.1 Calculation of Refractive Index and Reflectivity

Equations 10, 11, 12, 13, and 14 combine to describe the reflectivity of a surface for unpolarized light in terms of the grazing angle and the indices of refraction of both media. In this case, n_1 is assumed to be 1 as the photons begin in the air before reaching the reflective surface. According to Equation 2, n_r, the surface refractive index depends on both δ and β in the X-ray regime. δ and β are described by Equations 8, 9 in terms of their respective form factors. Figure 11 compares the National Institute of Standards and Technology (NIST) with Henke data for aluminum (Z = 13) f1 values for energies ranging from 2 keV to 433 keV. Focusing on the 20 to 433 keV range, this form factor is approximately constant at 13 e/atom.

The second form factor cannot be considered constant over this energy range. However, figure 12 shows the close relationship between NIST data and an interpolated power law fit over the chosen energy ranges. For both form factors, these approximations were used in the calculation of δ, β, n_r, and R.

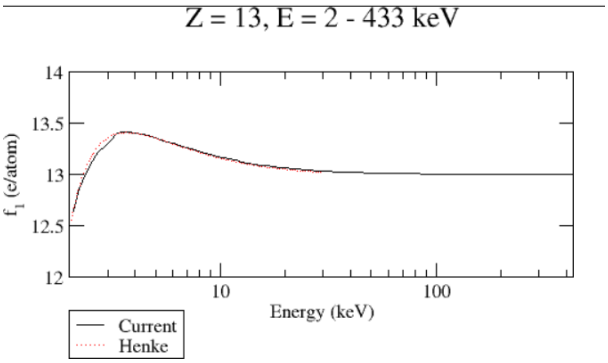

Figure 11: NIST experimental values of f1 vs energy for X-rays and gamma rays for Z=13. [2]

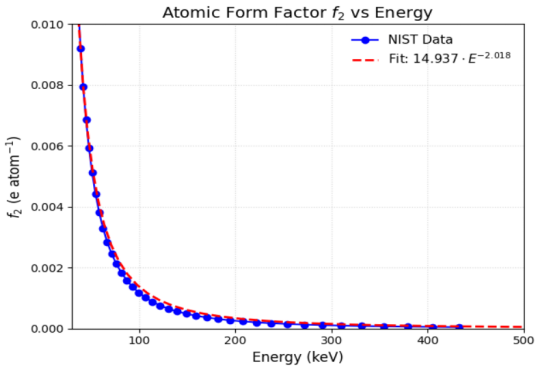

Figure 12: NIST experimental values of f2 vs energy for X-rays and gamma rays compared to interpolated power law fit for Z=13. [2]

5.2 Calculation of Roughness and Transmittance

Equation 16 combines the ideal roughness with the roughness component, known as the Névot-Croce factor [7]. Following this equation, an increase of roughness dampens the reflectivity curve. This is problematic not when gamma rays are allowed into the material but when X-rays are transmitted for high roughness values.

Figure 13 shows the reflectivity of the aluminum foil for a 100 keV photon at different grazing angles and roughness values as an example. Even on a nanometer roughness scale, the difference in reflectivity below the energy's critical angle is drastic and greatly varies from the total internal reflection in the ideal case.

5.3 Absorption Calculation

Equation 1 describes the exponential attenuation of photon intensity as a function of the path length through a material and the linear attenuation coefficient. Data for the attenuation coefficient μ are provided in the form of the mass attenuation coefficient μ/ρ (in m^2/kg in SI units), where ρ is the density of the material (in kg/m^3 in SI units).

The NIST data shown in Figure 14 along with Equation 1 can both be used to calculate the transmitted intensity ratio by linear interpolation between neighboring data points.

An additional factor to consider is the dependence of the absorbance on the grazing angle. As the grazing angle decreases, the path length increases according to the following

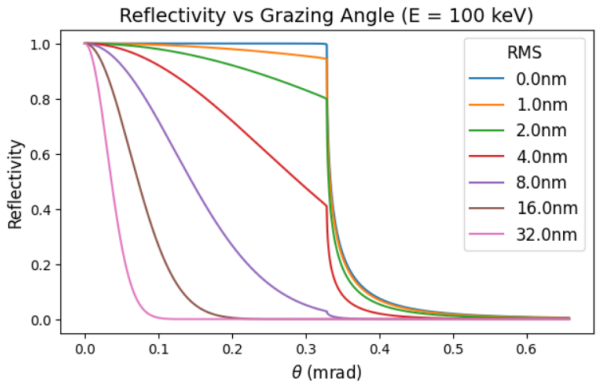

Figure 13: Reflectivity curves of 100 keV photons for different roughness values and grazing angles surrounding their critical angle: 329 nrad.

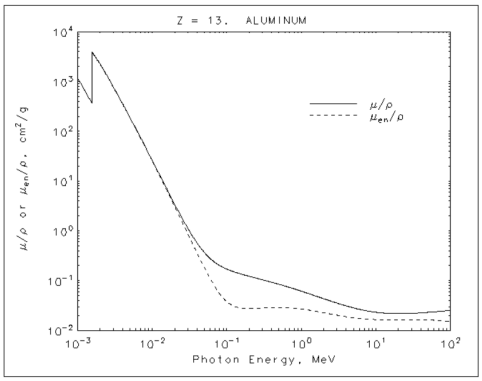

Figure 14: NIST data of Mass Attenuation Coefficients for X-rays and gamma rays [10].

equation:

$$x = \frac{t}{sin\theta} \tag{74}$$

where x is the path length, t is the membrane thickness, and θ is the grazing angle. Equation 74 assumes that $n_r \approx 1$, which is a safe assumption since the values of δ are on the order of not more than 10^{-6} and β are on the order of not more than 10^{-8} for the relevant energy range [4]. Therefore, the chosen angle has yet another limitation of the experiment as photons with energies of 100 keV and above are preferred to be transmitted. Although the angle needs to be small to effectively reflect X-rays, too small of an angle will cause too many gamma rays to be absorbed. The careful choice of the grazing angle is important for the selective energy-filtering mirror.

Following the trend of the Beer-Lambert law and Equation 74, Figure 15 has almost no transmittance for angles less than 0.01 mrad and almost 100% for angles greater than 10 mrad for a 100 keV photon and 2 micron thick foil. Figure 16 shows the percentage of photons that make it to each stage of the foil: entering, exiting, and both. The purple curve shows the product of the blue and green ones, representing the decreased probability of photons not being reflected or absorbed.

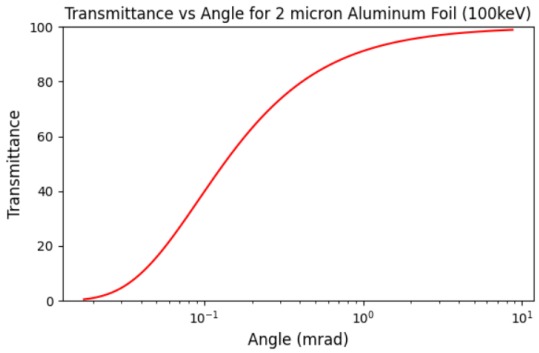

Figure 15: Transmittance percentage of 100 keV photons for different grazing angles assuming no reflectivity.

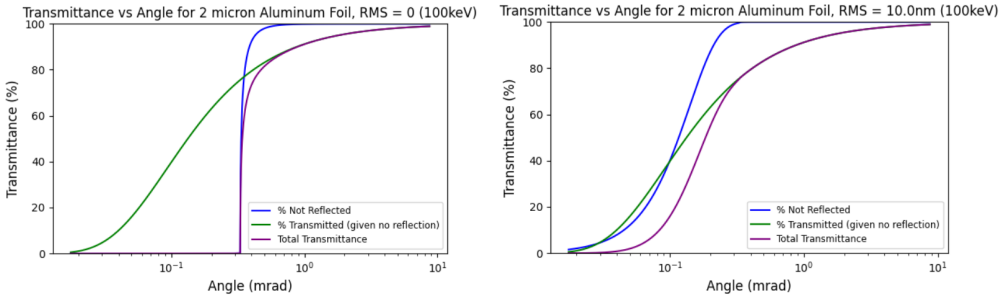

Figure 16: Percentage of 100 keV photons that enter the foil (blue), leave once inside (green), and both enter and exit (purple) over different grazing angles for $2\mu m$ thick aluminum foil for RMS=0 (left) and RMS=10 nm (right).

5.4 Calculating Grazing Angle

The grazing angle should be within a specific range depending on the foil thickness and cutoff energies. Figure 17 shows the curves similar to Figure 16 with the addition of another photon energy. The orange curve highlights the total transmittance of the highest acceptable X-ray energy, currently set at 100 keV arbitrarily. The chosen X-ray cutoff will depend on the minimum roughness able to be obtained along with comparing the priority of signal rates with minimizing mirror thickness. The purple curve highlights the total transmittance of the lowest desired gamma ray, which is set to 1 MeV because for higher energies Equation 3 and therefore Equations 8 and 9 do not hold. As discussed earlier, the true gamma-ray energy cutoff would be around 6 GeV as energies below this are experimentally discarded and considered background. The final difference from Figure 16 is the black curve, which is the difference between the purple and orange curves, or the total photon transmittance. Therefore, the range of desired grazing angle is set by the regions where the black curve is at its maximum. This range has an upper bound of the X-ray energy critical angle and a lower bound of the gamma-ray critical angle. However, the difference in total transmittance is not constant over this range, and whenever possible, the angle should trend to the higher end.

We cannot discuss the reflectivity of the 6 GeV gamma rays using these methods because other processes are dominant and not accounted for. Similarly, the data in Figure 14 end at 100 MeV, so it is possible that the mass attenuation coefficients for GeV do not follow the decreasing trend.

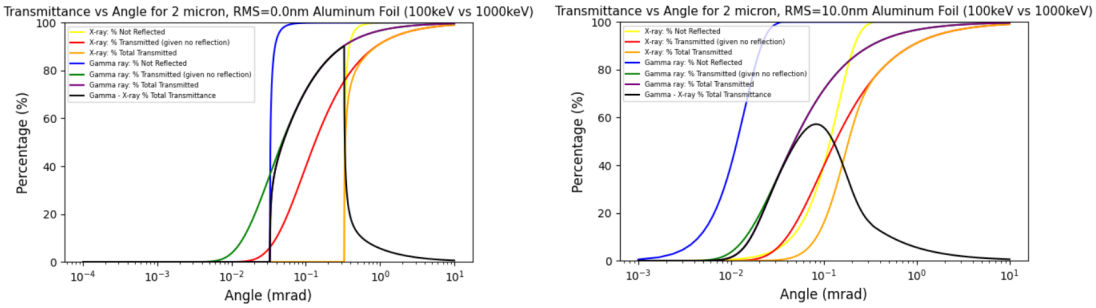

Figure 17: Percentage of 100 keV and 1 MeV photons that enter the foil (yellow, blue), leave once inside (red, green), and both enter and exit (orange, purple) over different grazing angles for 2μm thick aluminum foil for RMS=0 (upper) and RMS=10 nm (lower). The black curve shows the difference in the percentage of totally transmitted photons.

6 Results

The goal of the modified setup is to estimate the effect that unknown factors have on the tension of the thin membrane compared to the calculated value for a given mass.

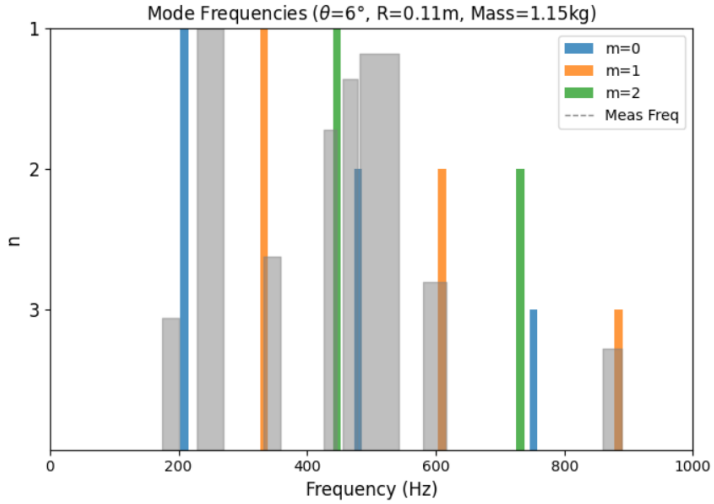

Figure 18: Theoretical (colored bars) and measured (gray) resonant mode frequencies for tense thin aluminum membrane.

Figure 18 contains the frequencies for which the circuit outputted a significant current spike to the oscilloscope to read (gray). During data collection, the gain of the electronic amplifier was set to 10^{-8} A/V. These discrete frequencies are then plotted alongside the calculated frequency modes for the circular membrane for a given mass (colored). While the y-axis for the theoretical modes represents the mode number n, for the measured values the y-axis describes the relative change in amplitude of the sinusoid at the given frequency.

The thickness of the gray bars was computed based on the reasonable range over which their maximum could be argued to lie based on the oscilloscope graph with an added 5 Hz of uncertainty due to the software for measuring frequency, Decibel X, jumping at intervals of 5 Hz at a time. The thicknesses of the colored bars were calculated based on error propagation of uncertainties in the membrane load, radius, density, angle (not grazing angle), and thickness.

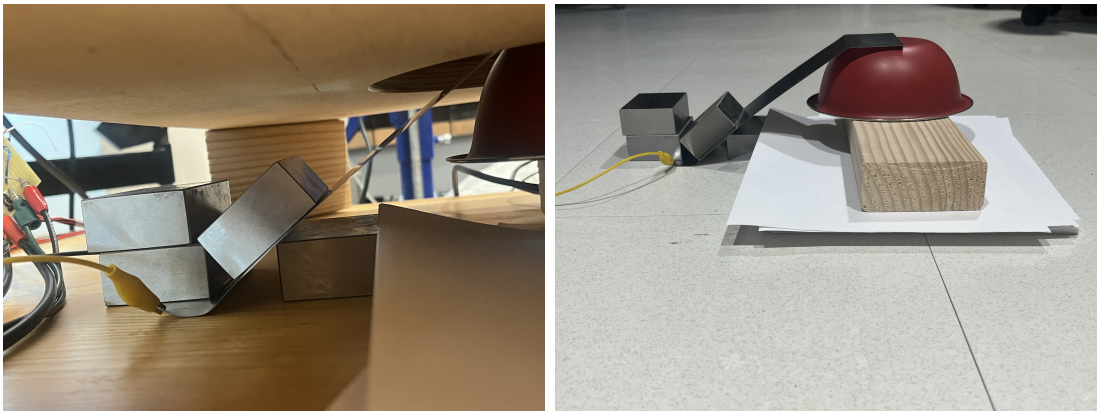

Figure 19: Images of improved system used for data collection both while assembled and deconstructed.

Many iterations were performed during the measurement process, as shown in Figure 19. A mass was added above and below the angled portion of the antenna to dampen its motion when its resonant modes are reached in the sweep. The height of a supporting bowl was controlled with wood and more finely with paper to minimize the capacitor plate separation.

Similarly, the speaker volume was set low enough so that the wooden supports and bowl no longer rattle and disrupt the stability of the system. During the frequency sweep after the final revisions to the system, there was no visible bouncing of the antenna.

6.1 Observations/Interpretations

Even after controlling the motion of the antenna, there were some complications reading the data off the oscilloscope. There is a decent amount of ambiguity in the frequency for which the oscilloscope outputs a maximum amplitude. The method of sweeping through the frequencies was a 10-minute linear sweep from 20 Hz to 20 kHz. The sweep was slow, but it was difficult to precisely pinpoint the exact resonant frequencies because of the continued sweep.

The relative change in amplitudes for the various maxima gives context as to whether the peak is building to a resonant mode, is one itself, or is due to an outside factor. The expectation is that all $m \neq 0$ modes result in no displacement current due to the symmetry of the system. Although the antenna has a rectangular shape, these modes are ignored as long as the antenna is perfectly centered. In addition, we expect the general trend of a decrease in maximum amplitude as the frequency increases. This trend is exacerbated by the relatively large size of the antenna that picks up cancellations in the $m=0$ modes as we increase n. The smaller the centered antenna, the more likely we are to be able to locate (4,0), for example.

7 Discussion

Based on the expectations and assumptions discussed, we can interpret the first peak as a build-up to the fundamental frequency or outside factors like the dampened motion of the antenna. The two largest peaks appear to correspond to the first and second $m=0$

modes. Despite the first peak being closer to the expected fundamental frequency, the relative heights give context to their origins.

An interesting phenomenon in Figure 18 is the absence of (3,0) with the presence of (3,1) modes. Although the amplitude should decrease significantly as n increases, it is unexpected to see the m = 1 peak for a constant n but not the m = 0 one. One possible explanation for this is the antenna misalignment. The misalignment has the potential to drastically change the influence of the modes, specifically the balance between the m = 0 and m = 1 modes. This is because for every millimeter in any direction the antenna is placed, the (1,1) mode membrane has a 2 mm change in the coverage difference between 'lowered' and 'raised' material and there can be less cancellation. This has the opposite effect on the m=0 modes, where they now have an increase in cancellation in their coverage. In this way, it is possible that the antenna was located in a position such that the (3,0) mode was balanced equally in its coverage while (3,1) was not. In the bottom right of Figure 6, the antenna appears to be aligned too far in one direction by several millimeters. Although this was discovered after the data was collected and the system was disassembled, this can be improved by securing the antenna before establishing the copper and membrane in place and adding weight.

The fourth and fifth peaks are likely due to build-up to the (2,0) peak. This is because the m = 2 amplitude is expected to be less than the m = 1 one despite the antenna being off center, so it is unlikely that either of these peaks are only from the (1,2) mode.

The main issue with Figure 18 is the disagreement of the second gray bar with the first blue one. This might suggest that there is something that influences the tension or location of the fundamental frequency under constant load that is not explained by Equations 66 and 3.5.

7.1 Future Improvements

The main improvement in this experiment would be to center and level the antenna with high accuracy. In addition, decreasing the size and changing to a circular shape will make the m=0 modes stand out even more above the rest. Securing the antenna to a physical stand and securing that to the table will ensure that there is no influence of the antenna's resonant modes on the displacement current.

Although not explicitly measured, the equilibrium distance between the two plates of the variable capacitor is around a couple millimeters. Decreasing this distance without risking any physical contact between the two surfaces would increase the overall visibility of the resonant modes. The camera should remain to spot any contact across the capacitor that leads to a short circuit.

Using improved software to analyze the frequencies would increase the precision of the measurements of resonant frequencies. Further trials should also be performed to increase this precision and increase confidence in whether external phenomena influence the result.

8 Conclusion

Once we have a strong understanding of how the membrane experiences low levels of tension, increasing the tension significantly can provide information on how 2-micron-thick aluminum is able to be stretched. The results suggest that unknown factors related to thin membranes do not dominate known contributors, but more research is needed to

provide more evidence of this. In addition, it is important to determine this balance of the factors that dominate for higher tensions. With information on how the thin membrane can be stretched, we can proceed with the differential thermal expansion process described in Section 3.4 with greater confidence when working with the extremely fragile film. Within a comfortable margin, the aluminum will be stretched with its yield limit in mind to minimize roughness. This roughness can then be measured to locate the ideal grazing angle using Figure 17 with the updated roughness value for installation in the GlueX detector.

9 Acknowledgments

I would like to thank both Richard Jones and James McIntyre for their invaluable support. Dr. Jones played a crucial role in my research journey, guiding me through every step of the process with patience and expertise. His mentorship helped me navigate the challenges and deepen my understanding of the subject. I am also grateful to James, who shared his own relevant experiences and provided a platform for exchanging ideas. Together, their contributions significantly enriched my research experience and helped me grow as a scholar. This work is supported by the U.S. National Science Foundation under grant 2209480.

References

[1] C. T. Chantler, "Theoretical Form Factor, Attenuation, and Scattering Tabulation for Z = 30–36, 60–89," *J. Phys. Chem. Ref. Data* **29**, 597 (2000).

[2] C. T. Chantler, K. Olsen, R. A. Dragoset, J. Chang, A. R. Kishore, S. A. Kotochigova, and D. S. Zucker, "Detailed Tabulation of Atomic Form Factors, Photoelectric Absorption and Scattering Cross Section, and Mass Attenuation Coefficients for Z = 1–92 from E = 1–10 eV to E = 0.4–1.0 MeV," National Institute of Standards and Technology (2001), https://physics.nist.gov/PhysRefData/FFast/html/form.html.

[3] Engineering ToolBox, "Linear Thermal Expansion Coefficients of Materials," (2003), https://www.engineeringtoolbox.com/linear-expansion-coefficients-d_95.html.

[4] B. L. Henke, E. M. Gullikson, and J. C. Davis, "X-Ray Interactions With Matter – Optical Constants Database," Lawrence Berkeley National Laboratory, https://henke.lbl.gov/optical_constants/getdb2.html.

[5] B. L. Henke, E. M. Gullikson, and J. C. Davis, "X-Ray Interactions: Photoabsorption, Scattering, Transmission, and Reflection at E = 50–30,000 eV, Z = 1–92," Lawrence Berkeley National Laboratory, https://henke.lbl.gov/.

[6] S. Adhikari *et al.*, "The GlueX Beamline and Detector," arXiv:2005.14272 [physics.ins-det] (2020).

[7] L. Névot and P. Croce, "Caractérisation des surfaces par réflexion rasante de rayons X. Application à l'étude du polissage de quelques verres silicates," *Rev. Phys. Appl.* **15**, 761 (1980).

[8] Advanced Research Instruments Corp., *PMT5R Current to Voltage Amplifier – Specifications*, http://www.aricorp.com/pdf/pmt5r.pdf.

[9] National Institute of Standards and Technology (NIST), "Thermal Expansion Coefficients," *J. Res. Natl. Bur. Stand.* **48**, 209 (1952), https://nvlpubs.nist.gov/nistpubs/jres/048/jresv48n3p209_a1b.pdf.

[10] J. H. Hubbell and S. M. Seltzer, "X-Ray Mass Attenuation Coefficients – Section 2," National Institute of Standards and Technology (NIST), https://physics.nist.gov/PhysRefData/XrayMassCoef/chap2.html.